Net Community Production and Inorganic Carbon Cycling in the Irminger Sea

M. F. Yoder[1], H. I. Palevsky[1], and K. E. Fogaren[1]

[1]Boston College, Department of Earth and Environmental Science.

Corresponding author: Meg Yoder (yoderma@bc.edu)

Key Points:

- We present the first multi-year, near-daily mixed layer dissolved inorganic carbon time series in the Irminger Sea
- Annual net community production within the seasonally varying mixed layer is high (9.7 ± 1.7 mol m^{-2} yr^{-1}) and has large interannual variability
- The greatest rates of inorganic carbon removal from the mixed layer via photosynthesis take place prior to mixed layer shoaling

Abstract

The subpolar North Atlantic plays an outsized role in the atmosphere-to-ocean carbon sink. The central Irminger Sea is home to well-documented deep winter convection and high phytoplankton production, which drive strong seasonal and interannual variability in regional carbon cycling. We use observational data from moored carbonate system chemistry sensors and annual turn-around cruise samples at the Ocean Observatories Initiative's Global Irminger Sea Array to construct a near-continuous time series of mixed layer dissolved inorganic carbon (DIC), pCO_2, and total alkalinity from summer 2015 to summer 2022. We use these carbonate system chemistry time series to deconvolve the physical and biological drivers of surface ocean carbon cycling in this region on seasonal, annual, and interannual time scales. We find high annual net community production within the seasonally-varying mixed layer, averaging 9.7±1.7 mol m^{-2} yr^{-1} with high interannual variability (range of 6.0 to 13.7 mol m^{-2} yr^{-1}). The highest daily net community production rates occur during the late winter and early spring, prior to the observed high chlorophyll concentrations associated with the spring phytoplankton bloom. As a result, the winter and early spring play a much larger role in biological carbon export from the mixed layer than traditionally thought.

Plain Language Summary

The subpolar North Atlantic takes in more carbon from the atmosphere than other areas of the ocean relative to its size. This is partially caused by photosynthesis in the surface ocean, which turns inorganic carbon into organic carbon that is transported into the deep ocean, a process known as the biological carbon pump. Using measurements from sensors on moorings in the Irminger Sea, we construct a seven-year time series of the different parts of the inorganic carbon system. Using these, we separate out the forces that impact how much inorganic carbon has the potential to be exchanged with the atmosphere. We find that biological processes remove inorganic carbon from the surface ocean in the spring, summer, and early fall, while in the winter the surface ocean gets deeper and encompasses waters from below that have higher carbon content. The total amount of inorganic carbon removed from the surface ocean each year by biological process is extremely high in the Irminger Sea compared to other global ocean regions. This research highlights the importance of long-term, full year measurements to understand carbon cycle dynamics.

1 Introduction

The ocean acts as a key sink in the global carbon cycle, absorbing carbon from the atmosphere at its surface and then storing it in the deep ocean. Different biological and physical factors work in tandem to drive this uptake. The biological carbon pump transports organic carbon produced via photosynthesis into the deep ocean, causing a decrease in surface ocean pCO_2 that results in carbon dioxide moving from atmosphere to ocean (DeVries, 2022; Volk & Hoffert, 1985). Globally, the biological carbon pump moves approximately 10 PgC yr^{-1} into the ocean interior and is the main contributor to the 40-fold difference between the ocean and atmosphere carbon reservoirs (Caldera et al., 2018; Friedlingstein et al., 2022; Siegel et al., 2023). The North Atlantic accounts for a disproportionately large share of this global export relative to its size, with estimates ranging from 0.55 to 1.94 PgC yr^{-1} (average 1.27 PgC yr^{-1}; Sanders et al., 2014). While extensive study has taken place in the North Atlantic on the myriad of pathways contributing to the region's biological carbon export, there is still high uncertainty in total flux values and the underlying mechanistic controls (Sanders et al., 2014).

Organic carbon meanders on its path from the surface to the deep ocean. It can be repeatedly aggregated, disaggregated, consumed, and respired by different classes of organisms, and is transported via sinking of particles, physical injection of high organic carbon waters, and vertical migration of heterotrophic grazers (Boyd, 2015; Boyd et al., 2019; Huang et al., 2022; Siegel et al., 2023; Stemmann & Boss, 2012). While known as the biological carbon pump, the physical processes involved in removing organic carbon from the surface cannot be siloed. In the North Atlantic, large spring phytoplankton blooms are thought to be the primary driver of high carbon export (Martin et al., 2011), however physical processes like deep convection have the potential to counterbalance this export by entraining previously exported carbon (Kortzinger et al., 2008; Palevsky & Nicholson, 2018; Quay et al., 2012, 2020). These dynamics are especially strong in the subpolar North Atlantic, which contains the deepest winter convection on Earth (de Jong et al., 2018; de Jong & de Steur, 2016; Holte et al., 2017) and high primary productivity (Boss & Behrenfeld, 2010; Henson et al., 2006, 2009).

To investigate the intertwined roles of biology and physics on carbon export, we use carbonate chemistry system measurements of dissolved inorganic carbon (DIC) and total alkalinity (TA) which provide mechanistically agnostic tracers of the removal and addition of carbon from the surface ocean. Net community production (NCP) is a measure of the net biologically produced organic carbon in the upper ocean. It can be determined using inorganic carbon measurements and when integrated throughout the year represents the biological pump on an annual basis (ANCP, Emerson, 2014). Marine carbon cycling has been studied around the globe by making inorganic carbon system measurements at regular intervals throughout the year since the early 1980's (Bates et al., 2014). However, these historic discrete shipboard measurements have not provided adequate temporal resolution to constrain the full seasonal and interannual variability influencing ANCP using carbonate chemistry (Bates et al., 2014; Racapé et al., 2013).

Technological advances since the turn of the century have increased observational capacity, providing high frequency time series measurements (more than once a day) for a number of chemical and physical parameters on both stationary mooring arrays and mobile floats and gliders. These have enabled the construction of DIC and TA mass balance budgets in the Northeast Atlantic, North Pacific, and Southern Ocean, and the subsequent disentanglement of biological and physical forcing on carbon cycling and quantification of annual net community production (Fassbender et al., 2016, 2017; Haskell et al., 2020; Huang et al., 2022; Knor et al., 2023; Kortzinger et al., 2008; Sauvé et al., 2023; Yang et al., 2021).

The Irminger Sea is an area of particular interest within the North Atlantic and is the location of the Global Irminger Sea Array (operated by the NSF's Ocean Observatories Initiative, OOI). The location was selected in order to provide sustained atmospheric, physical, and biogeochemical observations at a high latitude site, with a focus on the critical influences that affect the global ocean-atmosphere system (Fig 1., Ocean Observatories Initiative Science Prospectus, 2007; Smith et al., 2018). Fast moving currents bring water southward along the eastern coast of Greenland, and warm waters move northward along the eastern boundary as part of the North Atlantic current, forming the central Irminger Gyre where the array is located (de Jong et al., 2018). A 19-year time series (2002-2020) using OOI and nearby mooring data finds extreme variability in the depth of winter convection (285-1480 m, de Jong et al., 2024). Prior work in the region has used oxygen production as a tracer of photosynthesis and respiration (Palevsky & Nicholson, 2018) and the carbonate system seasonal cycle has been generally characterized (Bates et al., 2014; Racapé et al., 2013). As with many sites, there has not been sufficient data in the Irminger Sea to resolve full year-round net community production until now. Understanding the controls on the biological pump in subregions like the Irminger Sea contributes to our overall understanding of the North Atlantic's current carbon export and the potential changes it may undergo as a result of climate change, including changes in primary productivity, surface and deep ocean respiration, and physical transport. Here, we use seven years of high temporal frequency mooring data from the OOI Irminger Sea Array to provide the longest near-continuous daily carbonate chemistry dataset to date in this region. We leverage these data to determine the biological and physical forcing on carbon cycling and quantify net community production over seasonal, annual, and interannual time scales in the subpolar North Atlantic.

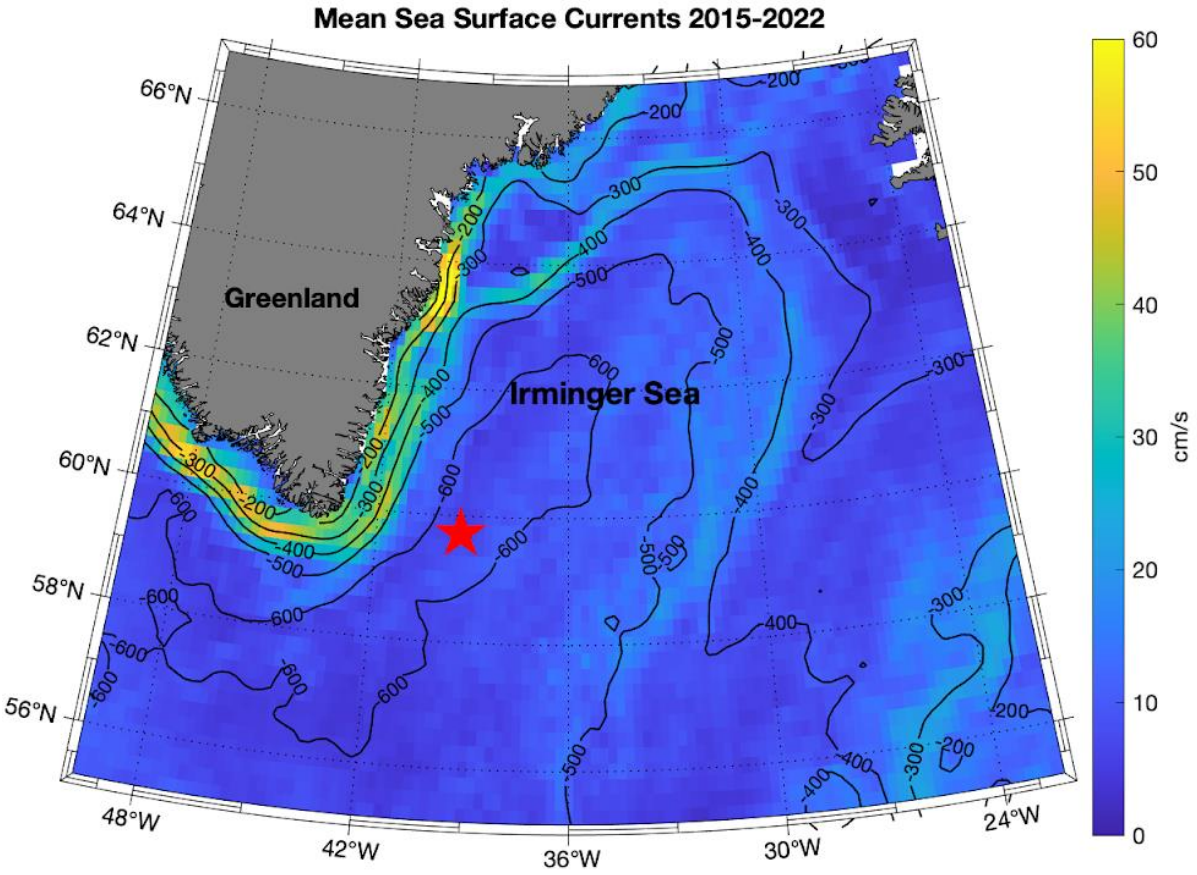

Figure 1. Map showing the Irminger Sea and location of Ocean Observatories Initiative Global Irminger Array (red star). The colored shading is the mean sea surface currents and the black contours are the mean sea surface height in millimeters for 2015-2022. Data are from E.U. Copernicus Marine Service Information, https://doi.org/10.48670/moi-00148.

2 Data

2.1 Ocean Observatories Initiative Global Irminger Sea Array

The Ocean Observatories Initiative (OOI) is a 25-year, NSF funded program that began collecting data in 2014, after nearly a decade of proposals and planning (Cowles et al., 2010; Isern & Clark, 2003; Smith et al., 2018). Our primary data source is the OOI Global Irminger Sea Array, which is comprised of 4 moorings, triangularly arranged and spaced approximately 20 km apart, and profiling and open ocean gliders (Fig. 2). Repeat hydrography at the mooring locations is also available from annual turn-around cruises. Our analysis focuses on the pH and pCO_2 sensors, all of which are located in the upper 130m of the water column, as well as their co-located CTDs.

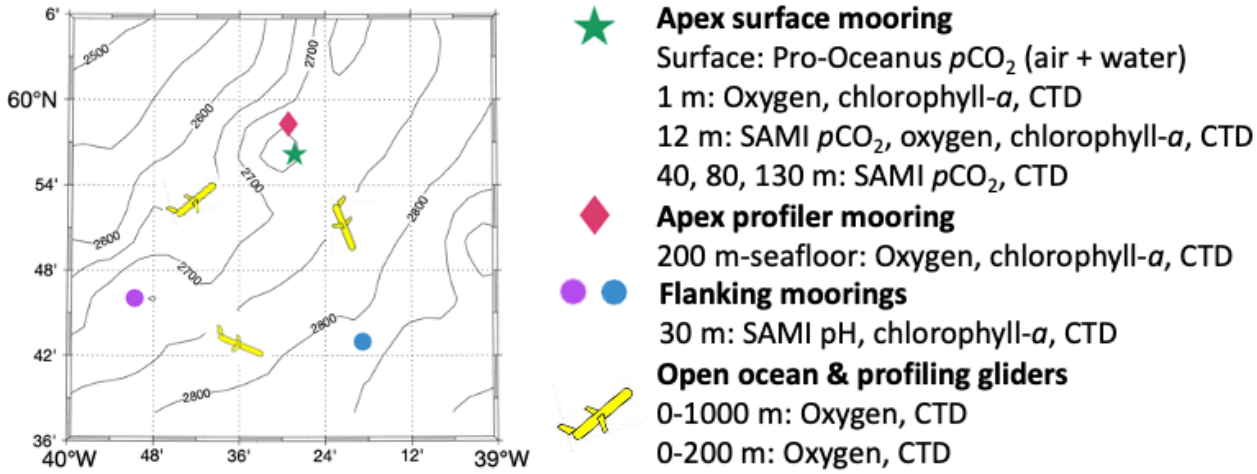

Figure 2. Schematic showing locations of the autonomous biogeochemical sensors and co-located CTDs on the OOI Irminger Array used in this analysis. Contour lines on the map show local bathymetry (m).

All carbonate system sensors, except at the surface, are Submersible Autonomous Moored Instruments (SAMI) made by Sunburst Sensors; both the pH and pCO_2 versions utilize spectrophotometry and a pH sensitive indicator dye (Álvarez et al., 2020; Lai et al., 2018). The surface pCO_2 sensor is a Pro-Oceanus CO_2-Pro, which operates above and below the water, making air and seawater measurements using infrared detection (Jiang et al., 2014). The pH and pCO_2 sensors below the surface make a measurement every 2 hours and the surface pCO_2 sensor makes a measurement every hour, though occasionally measurements are further apart due to battery limitations. Shallow sensors (pH sensors at 20m & 30m; pCO_2 sensors at 0m, 12m, & 40m) are in the mixed layer for the majority of the annual cycle, while deeper sensors (pH 100m, pCO_2 80m & 130m) are only in the mixed layer in the winter. The 20m and 100m pH sensors have very little usable data and have been excluded from this analysis.

147 pH and pCO_2 data were quality controlled using gross range and spike tests based on Quality
148 Assurance / Quality Control of Real Time Oceanographic Data (QARTOD) recommendations,
149 followed by a moving median filter (Palevsky et al., 2023; U.S. Integrated Ocean Observing
150 System, 2020; Table S1). We also remove data deemed suspect based on OOI operational
151 annotations (for further detail, see the OOI Biogeochemical Sensor Data Best Practices and User
152 Guide; Palevsky et al., 2023). The fixed asset data within the mixed layer for pH, pCO_2,
153 temperature, salinity, and pressure are at times sparse, with different depths and locations
154 available across the time series (Fig. S1 and S2). This sparsity is primarily due to infrastructure
155 and instrument failures, which tend to occur during the late winter when seas are extremely
156 rough and power becomes limited due to low sun angle. As a result, we have opted to combine
157 all carbonate system sensor data within the mixed layer in order to create the most complete time
158 series possible. Previous work has shown that the horizontal spatial variability is low enough to
159 analyze sensors across the array as one data stream (de Jong et al., 2018; Palevsky & Nicholson,
160 2018).

161 Beyond the upper ocean carbonate system chemistry and CTD sensors, we use calibrated oxygen
162 data from the wire-following profiler on the Apex profiler mooring (200-2000m, one cycle every
163 20 hours) and gliders (0-200m and 0-1000m, varying temporal coverage). These are corrected
164 using repeated stable deep oxygen measurements on the 3.1θ isotherm (~1800-2000m), based on
165 the approach previous applied at the Irminger Sea Array by Palevsky & Nicholson (2018). These
166 oxygen data are used for carbonate system predictions below the mixed layer using the
167 CONTENT model (Bittig et al., 2018). We also use chlorophyll-*a* data from Sea-Bird/WETLabs
168 fluorometers deployed on the OOI moorings at 1m, 12m, and 30m during periods they are within
169 the mixed layer. These data are presented for qualitative rather than quantitative interpretation, as
170 end-user quality control and calibration of the fluorometer data are beyond the scope of this
171 work.

172 2.2 Cruise Data

173 During the turn-around cruise each summer, discrete dissolved inorganic carbon (DIC), pH, and
174 total alkalinity (TA) samples are collected at depths corresponding to the deployment depths of
175 moored pH and pCO_2 sensors (Palevsky et al., 2023). In addition to the discrete samples
176 routinely collected and analyzed by the OOI program, we collected and analyzed additional DIC
177 and TA samples from the 2018 and 2019 turn-around cruises (Palevsky et al. 2023b). Quality
178 control of the discrete DIC, pH, and TA samples provided by the OOI program identified
179 inconsistencies among these three carbonate system chemistry variables that indicate data quality
180 issues with a subset of the TA samples. We therefore rely primarily on directly-measured
181 discrete DIC data rather than on other measured or calculated carbonate chemistry variables in
182 calibrating and validating the sensor-based time series. Our analysis also uses calibrated salinity,
183 temperature, and oxygen depth profiles from sensors on the CTD rosette (Fogaren et al., 2023;
184 McRaven, 2022a-d).

3 Methods

3.1 Carbonate System Time Series

We synthesize the fixed mooring assets to construct a near-continuous mixed layer carbonate system chemistry time series over the seven year period from summer 2015 through summer 2022. The mixed layer depth fluctuates significantly throughout the year, which results in the carbonate system sensors below the nominal 12m sensor alternating being in the mixed layer and below it, depending on their deployment depths and the current depth of mixing. For our mixed layer time series, we use only sensors deployed at nominally 40m and shallower; the process used to determine when sensors are in the mixed layer is described in Section 2 of the Supplementary Information (Fig. S3).

3.1.1 Total Alkalinity

Due to the close co-varying relationship between total alkalinity (TA) and salinity, regressions between the two have long been used to estimate total alkalinity for carbonate system calculations (Millero et al., 1998), with other variables having been incorporated in more recent work. We use the Locally Interpolated Alkalinity Regression (LIAR) model to predict TA from mixed layer sensor data, using temperature, salinity, and location as predictors (Carter et al., 2018).

3.1.2 Dissolved Inorganic Carbon

For each pCO_2 and pH sensor, DIC was calculated from daily averages of the sensor measurements and estimated total alkalinity (described above) using CO2SYS, with temperature, pressure, and salinity from co-located CTDs (Lewis & Wallace, 1998; Orr et al., 2018; van Heuven et al. 2011). Silicate and phosphate are also calculation inputs as they contribute to the acid-base system, however DIC outputs are very insensitive to these inputs (< 1 µmol kg^{-1} difference calculated using the minimum and maximum values ever recorded in the region). As a result, we use mean nutrient values from regional GLODAPv2_2021 data (Lauvset et al., 2021; Olsen et al., 2016). We used the dissociation constants of Lueker et al. (2000), the KSO_4 constant of Dickson (1990), and the total boron constant of Uppström (1974). Days with fewer than 2 measurements of pCO_2 or pH values are excluded. There are several short gaps in the time series where no carbonate system data is available. In the later part of the time series (summer 2018 - summer 2022) we fill these gaps using DIC predicted using CONTENT from the calibrated 1m and 12m moored oxygen sensors, with the longest gap being about 2 months in summer 2019 and all others being less than two weeks (Fig. S4).

3.1.3 Calibrating the DIC time series

Our use of a multitude of carbonate system chemistry sensors requires confirmation that these sensors are accurately measuring our parameters of interest. Once calibrated, the DIC time series calculated from individual sensors in the mixed layer match well with validation data from deeper moored assets as well as discrete cruise samples. The SAMI pCO_2 sensors show significant offsets from one another and from the Pro-Oceanus pCO_2 sensor during some deployments, but follow the same seasonal, weekly, and daily patterns when in the mixed layer (Fig. S5a). The SAMI pH sensors also show offsets, though much less substantial. The offsets between the SAMI sensors are not consistent annually, and there is no offset seen in the temperature data of the co-located CTDs, which indicates a known sensor calibration issue that require correction rather than a true signal (DeGrandpre et al., 2004; Kortzinger et al., 2008). The shallower pCO_2 and pH sensors (12-40m) used in the mixed layer time series are generally within a steep thermocline during turn-around cruises in summer, precluding aligning the moored sensor data with the discrete samples collected from co-located CTD casts as a calibration approach itself.

Unlike the SAMI sensors, when the Pro-Oceanus surface pCO_2 sensor measures for the entire deployment, the newly deployed sensor matches the previously deployed sensor while both are operational, which instills confidence in the accuracy of the surface Pro-Oceanus (summer 2020 and 2021, Fig. S1). The Pro-Oceanus, however, fails after only weeks to months in five out of the seven deployments used in this analysis. In order to create a complete mixed layer time series, we leverage the strengths of both carbonate chemistry sensor systems on the array, namely the longevity of the SAMI sensors and the accuracy of the Pro-Oceanus. We correct for offsets in the DIC time series calculated from the shallow (12-40m) SAMI pH and pCO_2 sensors by aligning them with the available DIC time series calculated from the Pro-Oceanus, after which we average all DIC data in the mixed layer (Supplementary Information Section 4, Fig. S5).

While we do not use the 80m and 130m pCO_2 sensor data as part of our mixed layer time series, they provide a useful check on our calibration process. The final mixed layer DIC time series shows good agreement with these deeper sensor DIC data, calibrated using predicted DIC from turn-around cruise CTD dissolved oxygen measurements, once they reenter the mixed layer (Fig. S5c, Bittig et al., 2018; Palevsky et al., 2023b). This agreement with the independently calibrated deep sensors, as well as with the available discrete cruise data points, further instills confidence in the choice to align the 12-40m DIC time series with the DIC time series from the Pro-Oceanus (Fig. S5c). A detailed explanation of the calibration processes can be found in Section 4 of the Supplementary Information.

3.1.4 pCO_2

We fill in the gaps in the surface pCO_2 record directly measured by the Pro-Oceanus using pCO_2 calculated from the mixed layer DIC time series, mixed layer estimated total alkalinity, salinity at 30m, and the fifth generation European Centre for Medium-Range Weather Forecasts atmospheric reanalysis (ERA5) sea surface temperature (Fig. S8, Hersbach et al., 2020). Salinity at 30m is used because there are frequent gaps in the surface pCO_2 record due to surface mooring platform failures, which also affected the co-located CTDs.

3.2 Mixed Layer Budget

Seasonal changes in the observed mixed layer DIC concentration are driven by physical transport, gas exchange, evaporation and precipitation, and biological processes, namely net community production and calcium carbonate production and dissolution (eq.1, Fassbender et al., 2016, 2017; Haskell et al., 2020; Kortzinger et al., 2008; Palevsky & Quay, 2017; Yang et al., 2021). Changes in total alkalinity are driven by the same processes as DIC, with the exception of gas exchange (eq. 2). The time rate of change terms for each tracer (left hand side of eq. 1 and 2, respectively) are determined from the DIC and TA time series data. Observational data allows us to calculate the non-biological drivers ($dDIC/dt_{Gas\ Exchange}$, $dDIC/dt_{EP}$, and $dDIC/dt_{Entrainment}$; dTA/dt_{EP}, and $dTA/dt_{Entrainment}$) and subtract from the weekly overall change ($dDIC/dt$; dTA/dt), leaving the biological drivers ($dDIC/dt_{Biology}$; $dTA/dt_{Biology}$), as the remainder. The sections below describe how each of the right hand side terms in these equations are calculated. All right-hand side terms in both budgets are calculated at weekly resolution. We smooth the observed carbonate system time series used in the budget with a three week running mean to remove high-frequency variability.

$$\frac{dDIC}{dt} = \frac{dDIC}{dt}_{|Gas\ Exchange} + \frac{dDIC}{dt}_{|EP} + \frac{dDIC}{dt}_{|Entrainment} + \frac{dDIC}{dt}_{|Biology} \quad (1)$$

$$\frac{dTA}{dt} = \frac{dTA}{dt}_{|EP} + \frac{d(TA}{dt}_{|Entrainment} + \frac{dTA}{dt}_{|Biology} \quad (2)$$

3.2.1 Gas Exchange

The rate of DIC change due to gas exchange is calculated from the measured partial pressure of carbon dioxide (pCO_2) in the atmosphere and surface waters, wind speed, temperature, and salinity, with positive values indicating a flux from the atmosphere into the ocean (eq. 3).

$$\frac{dDIC}{dt}_{|Gas\ Exchange} = k * K_H * \left(pCO_{2_{Air}} - pCO_{2_{Seawater}}\right) * \rho \quad (3)$$

The piston velocity (k) is calculated using the Ho et al. (2006) wind speed-dependent gas transfer parameterization, implemented in the MATLAB gas_toolbox (Manning and Nicholson, 2022) and the Schmidt constant (Wanninkhof, 1992). Of the OOI moored assets, the surface buoy faced the most challenges with continuous data collection, limiting the ability to use directly-measured meteorological data. Therefore, ERA5 products from the nearest grid cell (60˚N, 39.5˚W) are used for hourly sea surface temperature and 10m wind speeds (calculated from v- and u-winds at 10m, Hersbach et al., 2020). The ERA5 winds match well with the OOI 10m measured wind speeds, when available (Fig. S9).

The solubility of CO_2 is calculated using the temperature and salinity dependent constant (K_H) from Weiss (1974). The mixed layer seawater pCO_2 data is calculated as described in section 3.1.4. The air pCO_2 data is from NOAA's Global CarbonTracker gridded daily average product at 59˚N, 40.5˚W using CO_2 mole fraction, humidity, and barometric pressure (CT_2022 and CT-NRT.v2023-4, Jacobson et al., 2023, comparison with Pro-Oceanus air pCO_2, Fig. S10). Multiplying by the density (ρ) leaves us with the amount of carbon exchanged in units of mmol m^{-2} d^{-1}.

3.2.2 Physical Transport

The fixed nature of moored sensors necessitates a Eurlerian approach in order to account for the influence of horizontal and vertical transport on mixed layer DIC. The primary physical influence is entrainment, whereby the mixed layer increases in depth and adds water from below into the mixed layer. When the mixed layer shoals (detrainment), the mixed layer DIC concentration is not impacted. Given that this study site is in the center of the Irminger Gyre where there are low horizontal velocities, we exclude horizontal transport from our budget (Fig. 1). We also exclude estimating the budget contributions of vertical diffusion and vertical velocity. Although these have been shown to be significant in mixed layer mass balance budgets in other regions (such at North Pacific and North Pacific subtropical gyre, Fassbender et al. 2016; Knor et al. 2023), measured values for these terms have been shown to be low in the Irminger Sea and exceptionally deep winter convection at this site means that entrainment dominates over these second-order processes (Fratantoni, 2001; Painter et al., 2014; Våge et al., 2008).

In order to calculate the rate of physical entrainment, we use weekly mixed layer depths. There has been extensive discussion within the literature regarding how to define the mixed layer depth with respect to timescales of mixing and biological processes (Carranza et al., 2018; Carvalho et al., 2017; Lacour et al., 2019). We use a combination of methods including temperature thresholds and bio-optical methods to determine the mixed layer depth depending on the time of year and availability of both OOI and external data (Table S2), a full explanation of which can be found in the Supplementary Information, Section 6. We determine the effects of entrainment on mixed layer DIC, TA, and salinity using a one-dimensional model that accounts for the influence of mixing between the prior mixed layer and newly-entrained waters, calculated at weekly time steps. This model uses the mixed layer time series to calculate physical entrainment rates and accounts for the salinity, DIC, and TA of waters being entrained into the mixed layer using DIC and TA estimated from OOI glider and wire-following profiler oxygen, temperature, and salinity using the CONTENT model (Bittig et al., 2018). The entrainment model tracks closely with observed DIC concentrations in the fall, showing that the increase in mixed layer DIC during this period of time is primarily the result of the entrainment of high DIC waters (Fig. S12).

3.2.3 Evaporation and Precipitation

To account for dilution and concentration effects on DIC and TA due to evaporation and precipitation, we find the difference between the observed change in salinity over time and the entrainment-modeled change in salinity over time (Fassbender et al., 2016; Haskell et al., 2020).

We attribute the difference between the observations and the modeled change to evaporation and precipitation, as any change in salinity not due to entrainment is the result of these surface processes in our model, again assuming minimal horizontal advection. We multiply the difference in the two by the ratio of DIC (and TA) to absolute salinity on the first day of each deployment, working under the assumption that the ratio that salinity changes due to evaporation and precipitation is the same for DIC and TA (eq. 4). The same process is followed for TA.

$$\frac{d(DIC,TA)}{dt}_{|EP} = \left(\frac{dSal}{dt} - \frac{dSal}{dt}_{Entrainment}\right) * \frac{(DIC,TA)}{Sal}_{t=1} \quad (4)$$

3.2.4 Biological Processes

The biological drivers are calculated as the residual terms of equations 1 and 2. These drivers are net community production (NCP) via photosynthesis and respiration and calcium carbonate ($CaCO_3$) formation and dissolution (eq. 5).

$$\frac{d(DIC,TA)}{dt}_{|Biology} = \frac{d(DIC,TA)}{dt}_{|NCP} + \frac{d(DIC,TA)}{dt}_{|CaCO_3} \quad (5)$$

In order to separate the soft tissue processes (photosynthesis and respiration, which influence NCP) from calcium carbonate production and dissolution, we leverage the known production ratio of CO_2 and H^+ (117 to -17) from respiration using 1 mole of phosphate (HPO_4^{2-}) (Anderson & Sarmiento, 1994; Fassbender et al., 2016). This formation and precipitation of $CaCO_3$ influences TA and DIC in a 2:1 ratio. This allows us to calculate the influence of NCP on the mixed layer DIC budget (eq. 6). We also calculate weekly and annual NCP within the seasonally-varying mixed layer by integrating to the weekly mixed layer depth.

$$\frac{dDIC}{dt}_{|NCP} = \frac{\left(\frac{dTA}{dt}_{|Bio} - 2 * \frac{dDIC}{dt}_{|Bio}\right)}{-2 + \frac{-17}{117}} \quad (6)$$

3.3 Uncertainty

Here we present the calculated uncertainties of the calibrated DIC, TA, and pCO_2 time series, as well as uncertainties of terms in the DIC budget (Table 1). The uncertainties of the measured parameters propagated through to calculate these values can be found in the Supplementary Information (Table S3). Temperature and salinity measurement errors are slight but do factor into all of the calculated parameter uncertainties.

The uncertainty of the mooring DIC time series is estimated using the CO2SYS error propagation, with temperature, salinity, pressure, pH, pCO_2, and estimated TA uncertainties as inputs (Orr et al., 2018). Uncertainty for estimated TA is generated from the LIAR model (Carter et al., 2018). A limitation of deriving total alkalinity from salinity is that mixed layer TA can change independent of salinity when biological formation of calcium carbonate occurs. Remote sensing shows calcification rates exceeding 1 mmol C m^{-2} and very high interannual variability in calcification rates in the Irminger Sea, which could lead to our DIC estimates being slightly high in late summer (Hopkins et al., 2015). Despite this, the close agreement between the surface sensor pCO_2 and surface pCO_2 calculated from DIC and TA suggest that the impact of this uncertainty in TA is small (Fig. S8).

There is uncertainty in each of the terms of the mass balance budget (eq. 1 & 2, Table 1). The 95% confidence bounds of entrainment are calculated by taking the minimum and maximum values from the entrainment model runs with a combination of systematically over- and under-estimated mixed layer depths and the lower and upper uncertainties of the DIC concentration below the mixed layer. The evaporation-precipitation uncertainty is estimated using a Monte Carlo simulation iterated 5000 times with the salinity and DIC entrainment uncertainty and the uncertainty of the DIC concentration on the first week of each deployment. The gas exchange uncertainty is also calculated using a Monte Carlo simulation to account for the uncertainties in temperature, salinity, pCO_2 of air and seawater, and a 20% assigned uncertainty in the gas transfer coefficient to account for uncertainty in the wind speed data as well as in the parameterized relationship between wind speed and gas transfer (Ho et al., 2006; Wanninkhof, 2014; Yang et al., 2021). Calculating the biological processes as the remainder from the mass balance budget means that the biological term contains the accumulation of the uncertainties from all the other budget terms. We use a wrap-around Monte Carlo containing all the previously discussed uncertainties (Table 1) in which we subtract the physical transport, EP, and gas exchange terms from the overall change in DIC in order to determine the uncertainty in the biological processes.

399 Table 1.

400 *Uncertainties of analyzed parameters*

Time series	**Uncertainty**	**Primary sources of error**
Calibrated DIC ($\Delta DIC_{Observed}$)	11.2-11.6 mmol m^{-3}	Measurement of pH and pCO_2, calibration of DIC time series
TA ($\Delta TA_{Observed}$)	9.7-10.2 mmol m^{-3}	Estimate from LIAR model, measurement of salinity
pCO_2	2 µatm	Measurement of surface pCO_2, calculation from DIC and TA
$\Delta DIC_{Entrainment}$	8.7-10.3 mmol m^{-3}	DIC concentration below the mixed layer, mixed layer depth
ΔDIC_{EP}	1.1-2.0 mmol m^{-3}	entrainment salinity model from MLD and glider/WFP salinity measurements, ratio of DIC/TA to salinity on first day of deployment
ΔDIC_{GE}	0.02-0.05 mmol m^{-3}	air and sea pCO_2, wind speed, gas transfer coefficient
ΔDIC_{NCP}	14.7-16.0 mmol m^{-3}	Combined uncertainty of all other budget terms, stoichiometry of photosynthesis-respiration and calcium carbonate formation-dissolution
ΔDIC_{CaCO3}	28.5-30.5 mmol m^{-3}	Combined uncertainty of all other budget terms, stoichiometry of photosynthesis-respiration and calcium carbonate formation-dissolution

401 *Note.* Values shown are the range of yearly means over all seven years in the time-series.

4 Results and Discussion

4.1 Mixed layer time series

Here we present mixed layer carbonate system variables (DIC, TA, and pCO_2) as well as their potential drivers (mixed layer depth, temperature, and chlorophyll-*a*) in the central Irminger Sea (Fig. 3). The carbonate system variables follow a similar annual cycle of highs and lows, with the minimums occurring in late summer at the end of the productive season, then climbing throughout the fall to a maximum in winter, after which they are drawn down again in the spring (Fig. 3).

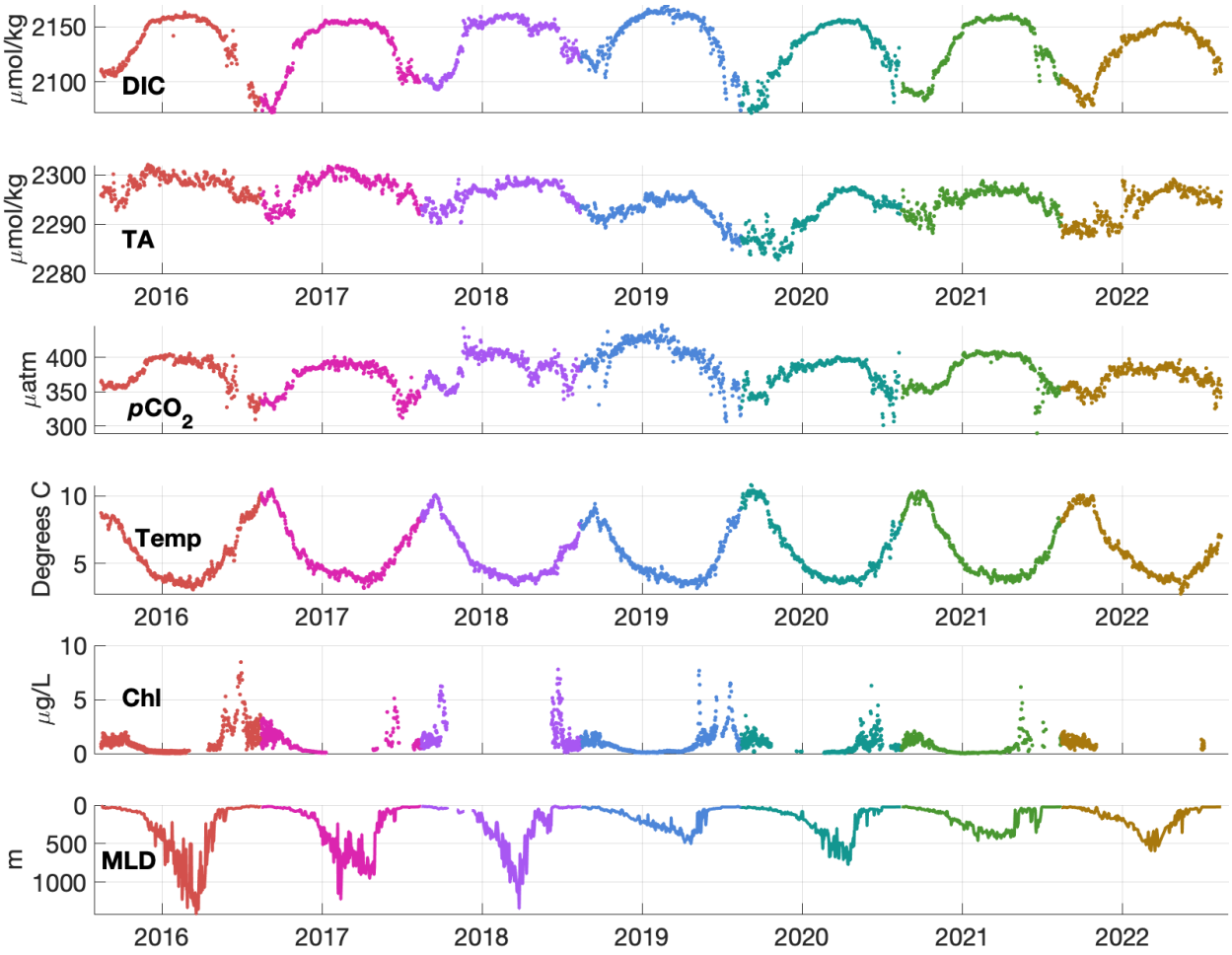

Figure 3. Daily mixed layer DIC, TA, pCO_2, temperature, chlorophyll-*a*, and mixed layer time series. Colors correspond with annual cycles beginning on August 15th.

In the Irminger Sea, sea surface temperatures vary significantly, from around 3˚C in the winter up to 12˚C in the summer. The partial pressure of CO_2 (pCO_2) is significantly affected by temperature (Weiss, 1974); if there were no biological processes reducing the pCO_2, we would expect to see the highest pCO_2 in the summer and the lowest pCO_2 in the winter, as solubility declines as temperature increases (Takahashi et al., 2002). Instead, as has been well documented in prior literature, the greatest pCO_2 are recorded in the winter and lowest are found in the summer due to biological drawdown, indicating that biophysical effects, rather than temperature, are the primary drivers of pCO_2 at our site (Bates et al., 2014; Landschützer et al., 2018; Takahashi et al., 2002).

The influence of vertical mixing and primary productivity can be clearly seen on the other, temperature-insensitive, carbonate system parameters (DIC and TA). In the spring and summer, the mixed layer is strongly stratified and high chlorophyll concentrations are recorded. At the same time, DIC concentrations reach their minimum in the annual cycle, ranging from 2074±8 to 2110±8 μmol kg^{-1} during our period of observation (Fig. 4). It is important to note that while chlorophyll concentration does indicate primary productivity, the amount of inorganic carbon being utilized is not directly reflected, as widely varying chlorophyll to carbon ratios occur at different global locations, depths in the water column, and times of year (Sathyendranath et al., 2009). Due to infrastructure failures, the sensors are not always successful in capturing the entire spring bloom; however, in situ chlorophyll measured by fluorometry and satellite chlorophyll data confirm annual spring and fall blooms at the Irminger site (Painter et al., 2014).

In the fall, convection begins and the mixed layer starts deepening. The Irminger Sea's uniquely deep mixed layers are not observed until later in the season, with mixed layer depths rarely exceeding 100m before mid November. Most of the interannual variability in mixed layer depth occurs in the winter, both in the timing of deepening and the maximum depth reached. Some years, such as 2015-2016, experience early and rapid deepening, but the deepest sustained winter mixing is usually reached in mid to late March, ranging from ~400 to ~1300m. The patterns observed here match previous analysis of MLDs in this region (de Jong et al. 2024). Shoaling in the spring begins gradually and then intensifies, going from near maximum depths to less than 100m over the span of a few weeks from early April to mid-May (Sterl and de Jong, 2022). During this time, we observe repeated shoaling and deepening, a process previously observed in the North Atlantic (Lacour et al., 2019). After the final shoaling, increased chlorophyll concentrations are observed again. It should be noted that the seven year OOI time series captures a period of time in which there is particularly strong winter convection (3 winters deeper than 1000m), even for the Irminger region. Before the OOI time series, winter mixed layer depths for only one year between 2002 and 2013 (2011-2012) were close to 1000m (de Jong et al., 2024).

The mixed layer DIC signal generally increases and decreases in concert with the seasonal changes in mixed layer depth. The increase in mixed layer DIC coincides with mixed layer deepening (Fig. 3). It is rapid in mid-September through mid-November and then continues to rise with a less significant slope between mid-February to late March, when it reaches the maximum annual concentration. The DIC concentration begins to decrease moderately in the late winter and then decreases more rapidly in late April to mid-May, coinciding with high chlorophyll concentrations.

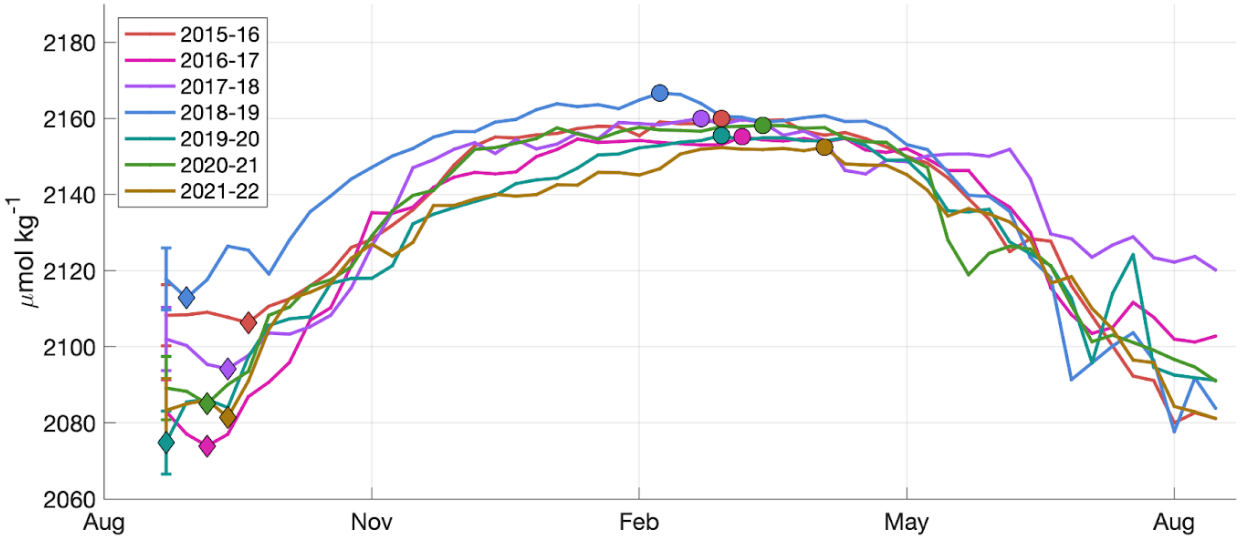

Figure 4. The annual seasonal cycle of DIC concentration in the mixed layer, beginning on August 15th. The diamonds are the lowest DIC concentration at the end of the productive season and the circles are the annual DIC maximum. The error bars at the beginning of the time series show uncertainty derived from the Monte Carlo simulation and apply across the time series. Gaps less than 2 weeks have been filled via linear interpolation.

The amount of fall-winter increase and spring-summer decrease of mixed layer DIC varies from year to year. While there is a broad interannual range in the amplitude of the DIC seasonal cycle (mean 68±11, range 54-81 µmol kg^{-1}), the range of the winter maximum weekly DIC concentration is only 14 µmol kg^{-1} (Fig. 4). This is almost within the uncertainty of the mixed layer DIC time series (~11 µmol kg^{-1}), making the annual maximum DIC effectively indistinguishable from year to year. The summer minimum is far more variable, reflecting more variability in the impact of biological DIC drawdown than winter convection on the mixed layer DIC annual cycle. The DIC seasonal cycle amplitude is similar to previous measurements in the Irminger Sea (~60 µmol kg^{-1}, Bates et al., 2014) and other high latitude regions including the North Pacific (~56±7 µmol kg^{-1} at Ocean Station Papa, 73±2 µmol kg^{-1} in the Kuroshio Extension, Fassbender et al., 2016, 2017) and Western Antarctic Peninsula (~55 µmol kg^{-1},Yang et al., 2021), however the interannual variability observed in the Irminger Sea is higher.

476 4.2 Mixed Layer Carbon Mass Balance

477 To investigate the specific drivers of the annual carbonate system chemistry cycle and its
478 interannual variability, we use a mass balance approach. Comparison among each of the terms
479 influencing the DIC seasonal cycle (eq. 1) shows that entrainment of deep waters and biological
480 processes have the greatest impact on the DIC seasonal cycle, with gas exchange and
481 evaporation-precipitation playing relatively minor roles (Fig. 5).

482

483

484

485

486

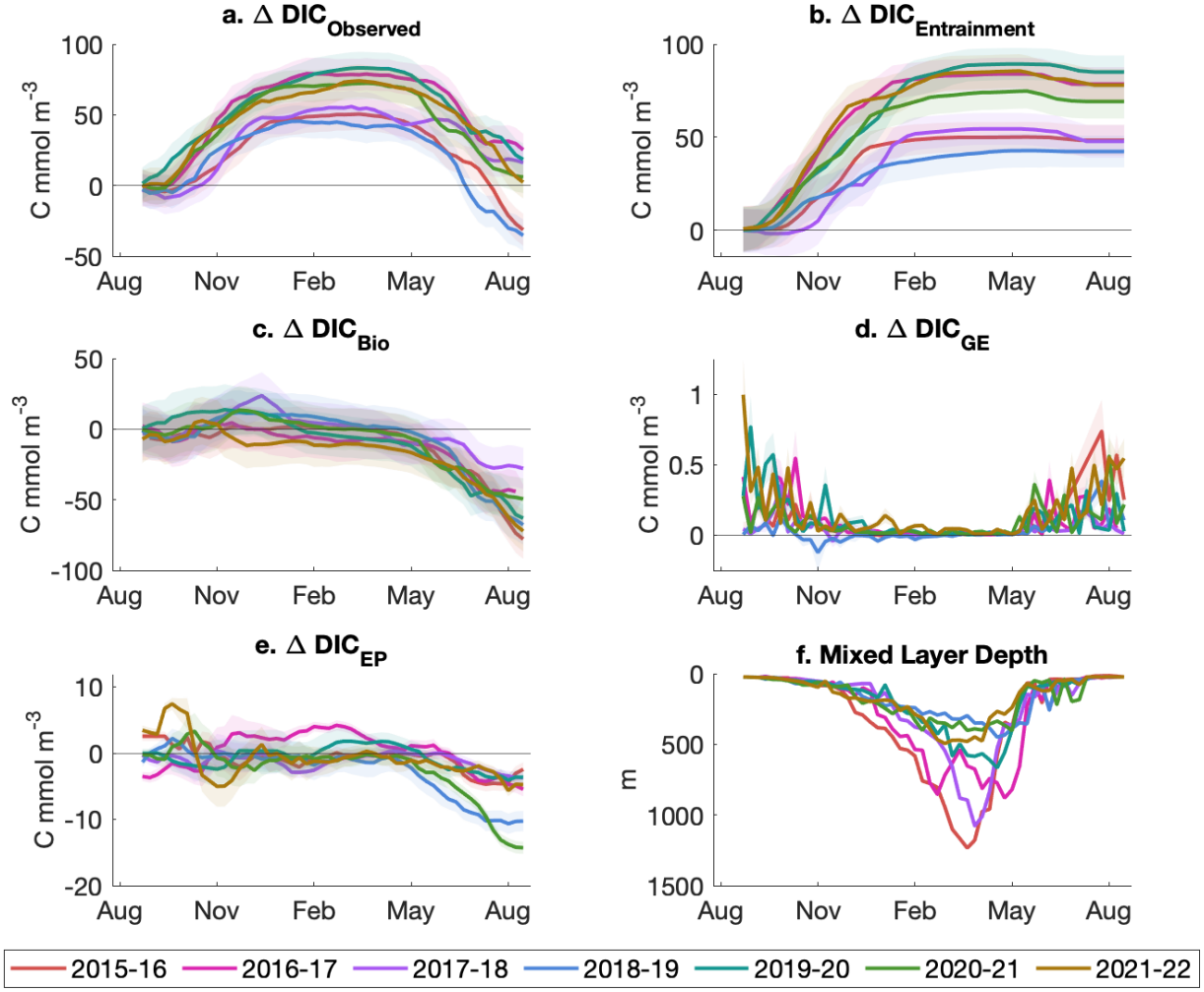

487

488 **Figure 5.** Influences of each term in the mixed layer DIC mass balance budget (eq. 1) on a) the
489 observed change in DIC concentration since Aug. 15 over each of the seven years in the time
490 series. Changes in mixed layer DIC are driven by: b) the change in DIC concentration due to
491 entrainment, c) the change in DIC concentration due to biological processes, d) the change in
492 DIC concentration due to gas exchange, and e) the change in DIC concentration due to
493 evaporation and precipitation, each presented as the cumulative change since August 15 in each
494 year of the time series. Each of these terms is calculated within the seasonally-varying mixed
495 layer depth at weekly resolution (f). Note that the y-axes are scaled differently on each plot.

While gas exchange has very little impact on the overall mixed layer DIC concentration, the average total addition of DIC to the mixed layer due to CO_2 influx from the atmosphere is 2.1 mol ± 1.1 mol m^{-2} yr^{-1} over our seven year period. A recent pCO_2 climatological product reports a mean of 3.0±0.7 mol m^{-2} yr^{-1} during our study period (range 2.1-3.8 mol m^{-2} yr^{-1}, Landschützer et al. 2020). This matches our observations within the uncertainty, and the somewhat higher values can likely be attributed to our differing choice of gas transfer parameterization (Atamanchuk et al., 2020). From our observational data, the years with the lowest annual carbon uptake via gas exchange are also the years when the maximum mixed layer depth exceeds 1000m (2015-2016 and 2017-2018), potentially indicating that the continued entrainment of high DIC waters suppresses winter uptake driven by cooling waters. Gas exchange occurs at the surface and therefore has the highest potential to impact DIC concentration when the mixed layer is shallowest (has the least volume). The most significant stratification occurs during the summer when the difference between air and seawater pCO_2 is greatest. These conditions would support strong influx; however the winds tend to be slow this time of year and do not drive vigorous gas exchange. In the winter when extremely high winds occur, the volume of the mixed layer has expanded by almost two orders of magnitude, so even the fastest gas exchange has very little impact on overall mixed layer DIC concentration, making gas exchange ($dDIC/dt_{GE}$) the least impactful driver of changes in mixed layer DIC (Fig. 5d).

514 The impact of evaporation and precipitation on DIC concentration ($dDIC/dt_{EP}$) is also low
515 throughout the year, and, as with gas exchange, has the greatest impact when the water column is
516 stratified due to its influence occurring only at the air-sea interface. The impact of evaporation
517 and precipitation varies from year to year but, on average, mild dilution occurs in the summer
518 months, reducing DIC concentration by 6.4 ± 4.3 mmol m^{-3} yr^{-1} (Fig. 5e). The dominant driver of
519 DIC increase in the mixed layer is entrainment ($dDIC/dt_{Entrainment}$), which increases mixed layer
520 DIC by 64±17 mmol m^{-3} yr^{-1}. The DIC concentration rises concurrently with an increase in
521 mixed layer depth as high DIC waters from below mix with the DIC-depleted surface waters.
522 The concentration rises rapidly even though the mixed layer does not deepen extremely quickly
523 because of the outsized role of the addition of water into the shallow end-of-summer mixed layer
524 and the very low summer DIC concentration. A mixed layer of 20m with DIC of 2080 mmol m^{-3}
525 that entrains 80m of 2170 mmol m^{-3} DIC waters then has a DIC concentration of 2152 mmol m^{-3},
526 an increase of 72 mmol m^{-3} and roughly the amplitude of the seasonal cycle. Alternatively, a
527 100m mixed layer with DIC of 2152 mmol m^{-3} that entrains 200m of 2170 mmol m^{-3} DIC waters
528 results in a DIC concentration of 2164 mmol m^{-3}, only increasing the overall concentration by 8
529 mmol m^{-3}. The total amount of carbon added via entrainment varies based on each year's
530 maximum mixed layer depth, but brings the surface concentration close to the same value each
531 winter (~2220 mmol m^{-3}). While we have primarily considered the extremely deep winter
532 convection for its role in returning carbon to the surface ocean in the winter, the subsequent
533 springtime shoaling of the mixed layer detrains water that contains both inorganic and organic
534 carbon in a process known as the seasonal mixed layer pump (Dall'Olmo et al., 2016). The
535 intraseasonal and seasonal mixed layer pump has been shown to significantly contribute to
536 carbon export in the subpolar North Atlantic, a process which is likely occurring at our study site
537 (Lacour et al., 2019).

538 Biological processes ($dDIC/dt_{Biology}$) lead to a net drawdown of DIC on an annual basis (Fig. 5c),
539 with photosynthesis and calcium carbonate formation outpacing respiration and calcium
540 carbonate dissolution. In the fall, the influence of biology is near zero, with slight heterotrophy in
541 some years and autotrophy in others; however, the uncertainty crosses zero most years,
542 obscuring any definitive fall trend. Each winter shows the same pattern: from February to May
543 there is a slow but persistent decrease in DIC concentration due to biological processes. Once the
544 mixed layer shoals, there is much more rapid drawdown, which comprises the bulk of the change
545 in concentration due to biology over the annual cycle. While we cannot quantitatively relate the
546 measured chlorophyll to DIC drawdown, the chlorophyll data clearly supports the rapid
547 reduction due to primary productivity in the late spring (Fig. 3).

548

549

550

4.3 Annual Net Community Production

The annual net community production (ANCP) within the mixed layer is the upper bound on the amount of carbon removed from the surface ocean by the biological pump each year (NCP = -ΔDIC_{NCP}). The choice of depth of integration for calculating ANCP varies depending on the method of export research. This can lead to discrepancies when intercomparing ANCP rates, particularly in high latitude regions with deep winter convection, where a significant fraction of the carbon removed from the mixed layer during spring and summer is subsequently respired within the seasonal thermocline and re-entrained into the mixed layer during winter (Palevsky & Doney, 2018). Here, we leverage our mixed layer DIC budget to determine the seasonal cycle and interannual variability of NCP and ANCP integrated to the seasonally varying mixed layer depth. While not all of this NCP will lead to long-term carbon sequestration at depth, this value is of particular interest as the surface ocean pCO_2, and in turn the influx of carbon from the atmosphere to the upper ocean, is strongly influenced by NCP-driven changes in mixed layer DIC concentration.

We find net autotrophy in the Irminger Sea for most of the year, with the highest NCP rates occurring in the early spring prior to mixed layer shoaling (Fig. 6). NCP rates in this paragraph are the mean and standard deviation across all 7 years. In the late summer into the late fall, we observe NCP from near neutral to mildly heterotrophic (-5±17 mmol m^{-2} d^{-1} from Aug. 15 to Nov. 15). In January, there is a transition to autotrophy with an NCP of 24±43 mmol m^{-2} d^{-1} until the end of February. By April, shoaling has begun and the mixed layer is strongly autotrophic, with an NCP of 77±26 mmol m^{-2} d^{-1} from the beginning of April to mid-May. From then until August 15th, the mixed layer is relatively shallow and continues to be autotrophic at a much lower NCP of 28±24 mmol m^{-2} d^{-1}.

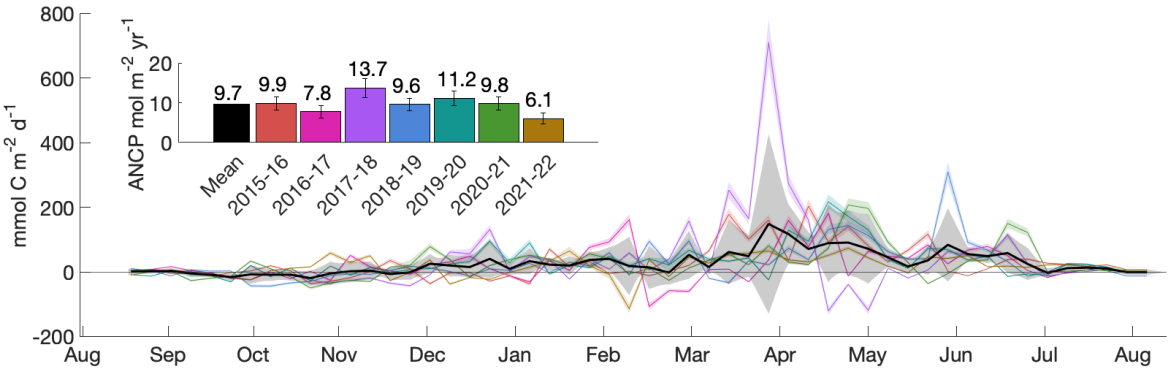

Figure 6. Net community production (NCP) rates integrated to the seasonally-varying mixed layer depth. The colored lines show each individual year, the thick black line shows the mean across all years, and the gray shading is one standard deviation of the interannual mean. The bar chart shows total annual net community production (ANCP). ANCP error bars are the uncertainty as calculated through Monte Carlo analysis (details in Section 3.3).

We find that the central Irminger Sea has high ANCP as well as high interannual variability, with an annual mean of 9.7±1.7 mol C m^{-2} yr^{-1} (± signifies propagated error, not standard deviation, Fig. 6). The highest ANCP recorded during our study period was 13.7±2.3 mol C m^{-2} yr^{-1} during 2017-2018. This year had a later-than-average onset of mixed layer deepening, resulting in a shallow fall mixed layer that caused the high fall chlorophyll concentration without a high depth-integrated rate of NCP. This is the only year with a decrease in DIC due to entrainment, likely indicating photosynthesis below the mixed layer during the large fall bloom. There is a late fall respiration signal, potentially fueled by sinking organic carbon from the fall bloom. 2017-2018 had very deep winter convection, as well as a decrease in DIC due to NCP from early March to mid-April that outpaced the time series mean (12 mmol m^{-3} reduction in DIC over this time period compared to the time series mean of 5 mmol m^{-3}), which together resulted in high integrated NCP over this time period and for the yearly total. The lowest ANCP recorded occurred during 2021-2022 (6.0±1.3 mol m^{-2} yr^{-1}), which also had the earliest spring shoaling of the observed period (Fig. 3). DIC increased in the late fall due to both entrainment and respiration and there were relatively low NCP rates in the winter and early spring. These findings indicate that the depth and timing of winter mixing substantially impacts the overall annual net community production; however the rate of DIC drawdown by biology prior to mixed layer shoaling is also an important control on ANCP.

This study adds to a growing body of research using DIC and TA as mass balance tracers to quantify ANCP within the seasonally varying mixed layer depth. The majority of sites have yielded lower ANCP than we find in the Irminger Sea (2±1 mol C m^{-2} yr^{-1} at in the North Pacific, 1.2±2.8 mol C m^{-2} yr^{-1} in the North Pacific subtropical gyre, and 2.8±2.4 mol C m^{-2} yr^{-1} on the West Antarctic Peninsula shelf; Fassbender et al., 2016; Knor et al., 2023; Yang et al., 2021). However, in the Kuroshio extension in the North Pacific, ANCP was 7±3 mol C m^{-2} yr^{-1} (Fassbender et al., 2017). The Kuroshio site has the deepest winter mixed layer depths of other sites where these methods have been used (up to 300m), and similarly to the Irminger Sea, there are extremely high NCP rates seen in early spring as a result. A mixed layer carbon budget in the eastern subpolar North Atlantic (Porcupine Abyssal Plain site, 49˚N, 16.5˚W) found NCP within the seasonally-varying mixed layer of 6.4±1.1 mol m^{-2} yr^{-1}, with over two thirds of the production occurring prior to the spring shoaling of the mixed layer, a similar seasonal partitioning and annual magnitude as at our site (Kortzinger et al., 2008). Kortzinger et al. also found that 40% of the carbon exported from the seasonally-varying mixed layer was subsequently offset by entrainment of respired carbon during deep winter mixing. Reduced ANCP when integrating to the winter mixed layer depth as compared to ANCP within the seasonally-varying mixed layer has been corroborated by oxygen budgets using data from across the subpolar North Atlantic (Quay et al., 2012, 2020). Given the uniquely deep winter mixing in the Irminger Sea, it will be important for future work to contextualize our ANCP results by determining what fraction of this NCP contributes to long-term carbon sequestration, as well as the mechanistic relationship between NCP-driven DIC-drawdown in the mixed layer and air-sea CO_2 flux.

Our chemical tracer approach cannot provide insight into the complex ecosystem level dynamics that likely contribute to the observed high interannual variability in ANCP, however there is a clear connection between strong convection and high ANCP. Prior work investigating interannual variability of phytoplankton productivity in the Irminger Sea based on satellite chlorophyll data (which therefore does not capture early spring NCP discussed here) found that the onset of elevated chlorophyll concentrations varies by as much as 30 days (Henson et al., 2006). Their analysis found that timing of spring mixed layer shoaling influenced the timing and magnitude of the spring bloom; stormier winters with a high number of days with gale-force winds in turn delayed spring stratification, corresponding to later onset of elevated chlorophyll and lower peak chlorophyll concentrations (Henson et al., 2006). However, our work shows significant DIC drawdown by NCP within the deep late winter-early spring mixed layer, prior to mixed layer shoaling and increase in surface chlorophyll concentrations. Our finding of elevated NCP during deep winter mixing is consistent with the disturbance-recovery spring bloom hypothesis, in which the decoupling of zooplankton predator and prey during deep mixing enables enhanced primary productivity due to relief of grazing pressure (Behrenfeld & Boss, 2014). Historically, increased light availability with a shoaling mixed layer has been thought to be the catalyst of increased phytoplankton growth (Sverdrup 1953), however more recent work has demonstrated that though high chlorophyll concentrations may be driven by this critical depth hypothesis, a combination of more complex ecosystem interactions caused by winter mixing are at play (Behrenfeld & Boss, 2014 and references within; Mignot et al., 2018). Our results suggest that deeper mixed layers in the later winter and early spring may actually drive higher ANCP, potentially the result of inhibition of grazing due to mixing.

5. Conclusions

This work constructs the first long term time series of the inorganic carbon system in the subpolar North Atlantic using daily measurements of the carbonate system. Strong biological drawdown is the primary removal mechanism of inorganic carbon from the mixed layer. Increases in mixed layer DIC are primarily controlled by entrainment of high DIC waters as the mixed layer deepens due to winter convection. Similar maximum DIC concentrations are found each winter despite interannual variability in winter mixing, implying that variations in the depth of winter convection do not drive wintertime mixed layer DIC concentrations. While previous analysis at this site has emphasized the role of deep winter mixing reintroducing respired carbon to the mixed layer that has been previously exported (Palevsky and Nicholson, 2018), we find that strong NCP in the late winter and early spring begins reducing DIC concentration prior to shoaling in all years, such that years with extremely deep convection actually drive higher ANCP from the seasonally-varying mixed layer than those with shallower convection. The highest rates of NCP occur prior to the appearance of high chlorophyll concentrations, highlighting the utility of in situ sensing of carbonate parameters rather than relying on chlorophyll measurements as a proxy for biological productivity in the mixed layer. It is probable that the detrainment of water containing freshly produced organic carbon in the spring contributes to a high magnitude of carbon export, a subject which warrants further exploration.

The average annual net community production within the seasonally-varying mixed layer is 9.7±1.7 mol C m^{-2} yr^{-1} and ranges from 6.0 to 13.7 mol C m^{-2} yr^{-1} over the 7-year study period. Sparsity of data often leads to averaging across multiple years in ocean biogeochemistry and specifically when determining ANCP, however doing so can blur the important differences from year to year in both the drivers and magnitude. Averaging across multiple years does not sufficiently capture the complex carbonate system dynamics in the central Irminger Sea, driven by high interannual variability of winter convection and primary productivity. Collecting observational data is both costly and challenging, however if only one year of data is collected or multiple years are averaged together, ANCP in areas with high interannual variability like the Irminger Sea will be misrepresented. This is highly relevant in the context of efforts to detect the emerging impacts of ongoing anthropogenic climate change on biogeochemical cycles relative to baseline natural variability (Henson et al. 2016). The intended 25-year time series of the OOI Irminger Array will provide more information about the interconnected physical and biogeochemical controls on interannual variability in ANCP, as well as potential long-term trends.

Acknowledgments

The Ocean Observatories Initiative (OOI) is a major facility fully funded by the National Science Foundation (NSF) under Cooperative Agreement No. 1743430, and the Woods Hole Oceanographic Institution OOI Program Office. We thank the many members of the OOI team, as well as the research vessels and crews for annual OOI Irminger Sea turn-around cruises, who have collected and disseminated this time-series dataset. Our work with these data, and collection and analysis of ancillary measurements during OOI turn-around cruises, was supported by the NSF under awards OCE-194607, OCE-1947970, and OCE-2338450.

Open Research

Data Availability

Ocean Observatories Initiative mooring and glider data used in this analysis are all from the THREDDS Gold Copy catalog (https://thredds.dataexplorer.oceanobservatories.org/thredds/catalog.html). Reference designators for each depth and deployment can be found in the OOI Data Explorer (https://oceanobservatories.org/knowledgebase/how-to-decipher-a-reference-designator/, https://dataexplorer.oceanobservatories.org/). OOI DIC and TA bottle samples were accessed through the OOI Alfresco portal (https://alfresco.oceanobservatories.org/alfresco/faces/jsp/browse/browse.jsp).

DIC and TA bottle samples run at Boston College can be accessed on the Biological and Chemical Oceanography Data Management Office Database (BCO-DMO, https://www.bco-dmo.org/dataset/904722). ERA5 Reanalysis hourly sea surface temperature and 10m wind speed data, used for mixed layer calculations and air-sea gas exchange, are from https://doi.org/10.24381/cds.adbb2d47. Sea surface height and current data used in Figure 1 are from E.U. Copernicus Marine Service Information, https://doi.org/10.48670/moi-00148. NOAA's CarbonTracker data, used in air-sea gas calculations, are from https://doi.org/10.15138/ffxv-2z26. Nutrient mean values at our site are from GLODAPv2_2021, accessible at https://www.ncei.noaa.gov/data/oceans/ncei/ocads/data/0237935/.

Software Availability

All analyses were conducted in MATLAB from MathWorks. Basic physical oceanographic conversions were done using the Gibbs SeaWater (GSW) Oceanographic Toolbox of TEOS-10, available at http://www.TEOS-10.org. Calculations within the carbonate chemistry system used CO2SYS.v2.1, available at https://zenodo.org/records/3952803#.X0kReGdKhTa. Predicted DIC and TA were determined using the CONTENT model, accessible at https://github.com/HCBScienceProducts/CANYON-B. Gas transfer parameterizations were calculated using the Gas_Toolbox, accessible at https://zenodo.org/records/545858.

References

Álvarez, M., Fajar, N. M., Carter, B. R., Guallart, E. F., Pérez, F. F., Woosley, R. J., & Murata, A. (2020). Global Ocean Spectrophotometric pH Assessment: Consistent Inconsistencies. *Environmental Science and Technology*, *54*(18), 10977–10988. https://doi.org/10.1021/acs.est.9b06932

Anderson, L. A., & Sarmiento, J. L. (1994). Redfield ratios of remineralization determined by nutrient data analysis. *Global Biogeochemical Cycles*, *8*(1), 65–80. https://doi.org/10.1029/93GB03318

Atamanchuk, D., Koelling, J., Send, U., & Wallace, D. W. R. (2020). Rapid transfer of oxygen to the deep ocean mediated by bubbles. *Nature Geoscience*, *13*(3), 232–237. https://doi.org/10.1038/s41561-020-0532-2

Bates, N. R., Astor, Y. M., Church, M. J., Currie, K., Dore, J. E., González-Dávila, M., Lorenzoni, L., Muller-Karger, F., Olafsson, J., & Santana-Casiano, J. M. (2014). A Time-Series View of Changing Surface Ocean Chemistry Due to Ocean Uptake of Anthropogenic CO_2 and Ocean Acidification. *Oceanography*, *27*(1), 126–141. https://doi.org/10.5670/oceanog.2014.16

Behrenfeld, M. J., & Boss, E. S. (2014). Resurrecting the ecological underpinnings of ocean plankton blooms. *Annual Review of Marine Science*, *6*, 167–194. https://doi.org/10.1146/annurev-marine-052913-021325

Bittig, H. C., Steinhoff, T., Claustre, H., Fiedler, B., Williams, N. L., Sauzède, R., Körtzinger, A., & Gattuso, J. P. (2018). An Alternative to Static Climatologies: Robust Estimation of Open Ocean CO_2 Variables and Nutrient Concentrations from T, S, and O_2 data using Bayesian Neural Networks. *Frontiers in Marine Science*, *5*(328), 1–29. https://doi.org/10.3389/fmars.2018.00328

Boss, E., & Behrenfeld, M. (2010). In situ evaluation of the initiation of the North Atlantic phytoplankton bloom. *Geophysical Research Letters*, *37*(18). https://doi.org/10.1029/2010GL044174

Boyd, P. W. (2015). Toward quantifying the response of the oceans' biological pump to climate change. *Frontiers in Marine Science*, *2*(OCT), 1–15. https://doi.org/10.3389/fmars.2015.00077

Boyd, P. W., Claustre, H., Levy, M., Siegel, D. A., & Weber, T. (2019). Multi-faceted particle pumps drive carbon sequestration in the ocean. Nature, 568(7752), 327–335. https://doi.org/10.1038/s41586-019-1098-2

Caldera, K., Akai, M., Brewer, P., Chen, B., Haugan, P., Iwama, T., Johnston, P., Kheshgi, H., Li, Q., Ohsumi, T., Pörtner, H., Sabine, C., Shirayama, Y., Thomson, J., Barry, J., & Hansen, L. (2018). IPCC Special Report on Carbon Dioxide Capture and Storage. In *IPCC Special Report on Carbon Dioxide Capture and Storage*. https://doi.org/10.1016/b978-1-85617-636-1.00012-2

Carranza, M. M., Gille, S. T., Franks, P. J. S., Johnson, K. S., Pinkel, R., & Girton, J. B. (2018). When Mixed Layers Are Not Mixed. Storm-Driven Mixing and Bio-optical Vertical Gradients in Mixed Layers of the Southern Ocean. *Journal of Geophysical Research: Oceans*, *123*(10), 7264–7289. https://doi.org/10.1029/2018JC014416

Carter, B. R., Feely, R. A., Williams, N. L., Dickson, A. G., Fong, M. B., & Takeshita, Y. (2018). Updated methods for global locally interpolated estimation of alkalinity, pH, and

nitrate. *Limnology and Oceanography: Methods*, *16*(2), 119–131. https://doi.org/10.1002/lom3.10232

Carvalho, F., Kohut, J., Oliver, M. J., & Schofield, O. (2017). Defining the ecologically relevant mixed-layer depth for Antarctica's coastal seas. *Geophysical Research Letters*, *44*(1), 338–345. https://doi.org/10.1002/2016GL071205

Cowles, T., Delaney, J., Orcutt, J., & Weller, R. (2010). The Ocean Observatories Initiative: Sustained Ocean Observing Across a Range of Spatial Scales. *Marine Technology Society Journal* , *44*(6), 54–64.

Dall'Olmo, G., Dingle, J., Polimene, L., Brewin, R. J. W., & Claustre, H. (2016). Substantial energy input to the mesopelagic ecosystem from the seasonal mixed-layer pump. *Nature Geoscience*, *9*(11), 820–823. https://doi.org/10.1038/ngeo2818

de Jong, F. M., Oltmanns, M., Karstensen, J., & de Steur, L. (2018). Deep Convection in the Irminger Sea Observed with a Dense Mooring Array. *Oceanography*, *31*(1), 50–59. https://doi.org/10.2307/26307787

de Jong, M. F., & de Steur, L. (2016). Strong winter cooling over the Irminger Sea in winter 2014–2015, exceptional deep convection, and the emergence of anomalously low SST. *Geophysical Research Letters*, *43*(13), 7106–7113. https://doi.org/10.1002/2016GL069596

de Jong, M. F., Fogaren, K. E., Le Bras, I., McRaven, L., & Palevsky, H. I. (2024, in review at JGR:Oceans). Convection in the central Irminger Sea: insights into variability and the roles of surface forcing and stratification from 19 years of high resolution mooring data. *Journal of Geophysical Research: Oceans*.

DeGrandpre, M. D., Wanninkhof, R., McGillis, W. R., & Strutton, P. G. (2004). A Lagrangian study of surface pCO_2 dynamics in the eastern equatorial Pacific Ocean. *Journal of Geophysical Research: Oceans*, *109*(8). https://doi.org/10.1029/2003JC002089

DeVries, T. (2022). The Ocean Carbon Cycle. *Annual Review of Environment and Resources*, *47*, 317–341. https://doi.org/10.1146/annurev-environ-120920

Dickson, A. G. (1990). Thermodynamics of the dissociation of boric acid in synthetic seawater from 273.15 to 318.15 K. *Deep-Sea Research* , *37*(5), 755–766.

Emerson, S. (2014). Annual net community production and the biological carbon flux in the ocean. *Global Biogeochemical Cycles*, *28*, 1–12. https://doi.org/10.1002/2013GB004680

Fassbender, A. J., Sabine, C. L., & Cronin, M. F. (2016). Net community production and calcification from 7 years of NOAA Station Papa Mooring measurements. *Global Biogeochemical Cycles*, *30*, 250–267. https://doi.org/10.1002/2015GB005205.Received

Fassbender, A. J., Sabine, C. L., Cronin, M. F., & Sutton, A. J. (2017). Mixed-layer carbon cycling at the Kuroshio Extension Observatory. *Global Biogeochemical Cycles*, *31*(2), 272–288. https://doi.org/10.1002/2016GB005547

Fratantoni, D. M. (2001). North Atlantic surface circulation during the 1990's observed with satellite-tracked drifters. *Journal of Geophysical Research: Oceans*, *106*(C10), 22067–22093. https://doi.org/10.1029/2000jc000730

Friedlingstein, P., O'Sullivan, M., Jones, M. W., Andrew, R. M., Gregor, L., Hauck, J., Le Quéré, C., Luijkx, I. T., Olsen, A., Peters, G. P., Peters, W., Pongratz, J., Schwingshackl, C., Sitch, S., Canadell, J. G., Ciais, P., Jackson, R. B., Alin, S. R., Alkama, R., … Zheng, B. (2022). Global Carbon Budget 2022. *Earth System Science Data*, *14*(11), 4811–4900. https://doi.org/10.5194/essd-14-4811-2022

Fogaren, K. E., Palevsky, H. I. (2023) Bottle-calibrated dissolved oxygen profiles from yearly turn-around cruises for the Ocean Observations Initiative (OOI) Irminger Sea Array 2014 –

2022. Biological and Chemical Oceanography Data Management Office (BCO-DMO). (Version 1) Version Date 2023-07-19. doi:10.26008/1912/bco-dmo.904721.1

Global Ocean Gridded L4 Sea Surface Heights And Derived Variables Reprocessed 1993-Ongoing. *E.U. Copernicus Marine Service Information (CMEMS). Marine Data Store (MDS).* DOI: 10.48670/moi-00148 (Accessed on 08-Aug-2023)

Haskell, W. Z., Fassbender, A. J., Long, J. S., & Plant, J. N. (2020). Annual Net Community Production of Particulate and Dissolved Organic Carbon From a Decade of Biogeochemical Profiling Float Observations in the Northeast Pacific. *Global Biogeochemical Cycles*, *34*(10), 1–22. https://doi.org/10.1029/2020GB006599

Henson, S. A., Dunne, J. P., & Sarmiento, J. L. (2009). Decadal variability in North Atlantic phytoplankton blooms. *Journal of Geophysical Research: Oceans*, *114*(4), 1–11. https://doi.org/10.1029/2008JC005139

Henson, S. A., Robinson, I., Allen, J. T., & Waniek, J. J. (2006). Effect of meteorological conditions on interannual variability in timing and magnitude of the spring bloom in the Irminger Basin, North Atlantic. *Deep-Sea Research Part I: Oceanographic Research Papers*, *53*(10), 1601–1615. https://doi.org/10.1016/j.dsr.2006.07.009

Henson, S. A., Beaulieu, C., & Lampitt, R. (2016). Observing climate change trends in ocean biogeochemistry: When and where. Global Change Biology, 22(4), 1561–1571. https://doi.org/10.1111/gcb.13152

Hersbach, H., Bell, B., Berrisford, P., Hirahara, S., Horányi, A., Muñoz-Sabater, J., Nicolas, J., Peubey, C., Radu, R., Schepers, D., Simmons, A., Soci, C., Abdalla, S., Abellan, X., Balsamo, G., Bechtold, P., Biavati, G., Bidlot, J., Bonavita, M., … Thépaut, J. N. (2020). The ERA5 global reanalysis. *Quarterly Journal of the Royal Meteorological Society*, *146*(730), 1999–2049. https://doi.org/10.1002/qj.3803

Hersbach, H., Bell, B., Berrisford, P., Biavati, G., Horányi, A., Muñoz Sabater, J., Nicolas, J., Peubey, C., Radu, R., Rozum, I., Schepers, D., Simmons, A., Soci, C., Dee, D., Thépaut, J-N. (2023): ERA5 hourly data on single levels from 1940 to present. [Dataset]. Copernicus Climate Change Service (C3S) Climate Data Store (CDS), DOI: 10.24381/cds.adbb2d47 (Accessed on 13-Jul-2023)

Ho, D. T., Law, C. S., Smith, M. J., Schlosser, P., Harvey, M., & Hill, P. (2006). Measurements of air-sea gas exchange at high wind speeds in the Southern Ocean: Implications for global parameterizations. *Geophysical Research Letters*, *33*(16), 1–6. https://doi.org/10.1029/2006GL026817

Holte, J., Talley, L. D., Gilson, J., & Roemmich, D. (2017). An Argo mixed layer climatology and database. *Geophysical Research Letters*, *44*(11), 5618–5626. https://doi.org/10.1002/2017GL073426

Hopkins, J., Henson, S. A., Painter, S. C., Tyrrell, T., & Poulton, A. J. (2015). Phenological characteristics of global coccolithophore blooms. *Global Biogeochemical Cycles*, *29*(2), 239–253. https://doi.org/10.1002/2014GB004919

Huang, Y., Fassbender, A. J., Long, J. S., Johannessen, S., & Bif, M. B. (2022). Partitioning the Export of Distinct Biogenic Carbon Pools in the Northeast Pacific Ocean Using a Biogeochemical Profiling Float. *Global Biogeochemical Cycles*, *36*(2), 1–19. https://doi.org/10.1029/2021GB007178

Isern, A. R., & Clark, H. L. (2003). The Ocean Observatories Initiative: A Continued Presence for Interactive Ocean Research. *Marine Technology Society Journal* , *37*(3), 26–41. http://www.neptune.washington.edu

Jacobson, A. R., Schuldt, K. N., Arlyn Andrews, Miller, J. B., Oda, T., Sourish Basu, Mund, J., Weir, B., Ott, L., Aalto, T., Abshire, J. B., Aikin, K., Aoki, S., Allen, G., Apadula, F., Arnold, S., Baier, B., Bakwin, P., Bäni, L., … Miroslaw Zimnoch. (2023). *CarbonTracker CT-NRT.v2023-5*. NOAA Global Monitoring Laboratory. https://doi.org/10.15138/FFXV-2Z26

Jiang, Z. P., Hydes, D. J., Hartman, S. E., Hartman, M. C., Campbell, J. M., Johnson, B. D., Schofield, B., Turk, D., Wallace, D., Burt, W. J., Thomas, H., Cosca, C., & Feely, R. (2014). Application and assessment of a membrane-based pCO_2 sensor under field and laboratory conditions. *Limnology and Oceanography: Methods*, *12*(APR), 264–280. https://doi.org/10.4319/lom.2014.12.264

Knor, L. A. C. M., Sabine, C. L., Sutton, A. J., White, A. E., Potemra, J., & Weller, R. A. (2023). Quantifying Net Community Production and Calcification at Station ALOHA Near Hawai'i: Insights and Limitations From a Dual Tracer Carbon Budget Approach. *Global Biogeochemical Cycles*, *37*(7), 1–22. https://doi.org/10.1029/2022GB007672

Kortzinger, A., Send, U., Lampitt, R. S., Hartman, S., Wallace, D. W. R., Karstensen, J., Villagarcia, M. G., Llinás, O., & DeGrandpre, M. D. (2008). The seasonal pCO_2 cycle at 49°N/16.5°W in the northeastern Atlantic Ocean and what it tells us about biological productivity. *Journal of Geophysical Research*, *113*, 1–15. https://doi.org/10.1029/2007JC004347

Lacour, L., Briggs, N., Claustre, H., Ardyna, M., & Dall'Olmo, G. (2019). The Intraseasonal Dynamics of the Mixed Layer Pump in the Subpolar North Atlantic Ocean: A Biogeochemical-Argo Float Approach. *Global Biogeochemical Cycles*, *33*(3), 266–281. https://doi.org/10.1029/2018GB005997

Lai, C. Z., DeGrandpre, M. D., & Darlington, R. C. (2018). Autonomous optofluidic chemical analyzers for marine applications: Insights from the Submersible Autonomous Moored Instruments (SAMI) for pH and pCO_2. *Frontiers in Marine Science*, *4*(JAN), 1–11. https://doi.org/10.3389/fmars.2017.00438

Landschützer, P., Gruber, N., Bakker, D. C. E., Stemmler, I., & Six, K. D. (2018). Strengthening seasonal marine CO_2 variations due to increasing atmospheric CO_2. *Nature Climate Change*, *8*(2), 146–150. https://doi.org/10.1038/s41558-017-0057-x

Landschützer, Peter; Laruelle, Goulven G.; Roobaert, Alizée; Regnier, Pierre (2020). A combined global ocean pCO_2 climatology combining open ocean and coastal areas (NCEI Accession 0209633). NOAA National Centers for Environmental Information. Dataset. https://doi.org/10.25921/qb25-f418. Accessed April 17, 2023.

Lauvset, S. K., Lange, N., Tanhua, T., Bittig, H. C., Olsen, A., Kozyr, A., Álvarez, M., Becker, S., Brown, P. J., Carter, B. R., Cotrim Da Cunha, L., Feely, R. A., Van Heuven, S., Hoppema, M., Ishii, M., Jeansson, E., Jutterström, S., Jones, S. D., Karlsen, M. K., … Key, R. M. (2021). An updated version of the global interior ocean biogeochemical data product, GLODAPv2.2021. *Earth System Science Data*, *13*(12), 5565–5589. https://doi.org/10.5194/essd-13-5565-2021

Lewis, E. R., & Wallace, D. W. R. (1998). Program Developed for CO_2 System Calculations. In *ESS-DIVE*. Environmental System Science Data Infrastructure for a Virtual Ecosystem. https://doi.org/https://doi.org/10.15485/1464255

Lueker, T. J., Dickson, A. G., & Keeling, C. D. (2000). Ocean pCO_2 calculated from dissolved inorganic carbon, alkalinity, and equations for K1 and K2: validation based on laboratory

measurements of CO_2 in gas and seawater at equilibrium. *Marine Chemistry*, *70*(1–3), 105–119. https://doi.org/10.1016/S0304-4203(00)00022-0

Manning, C.C.M. and D.P. Nicholson (2022). dnicholson/gas_toolbox: MATLAB code for calculating gas fluxes. Zenodo. https://doi.org/10.5281/zenodo.6126685

Martin, P., Lampitt, R. S., Jane Perry, M., Sanders, R., Lee, C., & D'Asaro, E. (2011). Export and mesopelagic particle flux during a North Atlantic spring diatom bloom. *Deep-Sea Research Part I: Oceanographic Research Papers*, *58*(4), 338–349. https://doi.org/10.1016/j.dsr.2011.01.006

McRaven, L. (2022a). Water temperature, salinity, and others taken by CTD and Niskin bottles from the research vessel Neil Armstrong in the North Atlantic Ocean during 2020 Ocean Observations Initiative (OOI) Irminger Sea 7 and Overturning in the Subpolar North Atlantic Program – Greenland Deep Western Boundary Current, ONSAP-GDWBC, cruise AR46 from 2020-08-08 to 2020-08-26. (NCEI Accession 0252117) [Data set]. NOAA National Centers for Environmental Information. https://doi.org/10.25921/51B4-AC30 https://doi.org/10.25921/51b4-ac30

McRaven, L. (2022b). Water temperature, salinity, and others taken by CTD and Niskin bottles from the research vessel Neil Armstrong, Irminger Sea 5 cruise AR30-03, in the North Atlantic from 2018-06-06 to 2018-06-22. (NCEI Accession 0252116) [Data set]. NOAA National Centers for Environmental Information. https://doi.org/10.25921/BFSV-YP35 https://doi.org/10.25921/bfsv-yp35

McRaven, L. (2022c). Water temperature, salinity, and others taken by CTD and Niskin bottles from the research vessel Neil Armstrong, cruise AR35-05, in the North Atlantic from 08-02-2019 to 08-25-2019 (NCEI Accession 0251721) [Data set]. NOAA National Centers for Environmental Information. https://doi.org/10.25921/61KN-QV10 https://doi.org/10.25921/61kn-qv10

McRaven, L. (2022d). Water temperature, salinity, and others taken by CTD and Niskin bottles from the research vessel Neil Armstrong, cruise AR60-01, in the North Atlantic from 08-03-2021 to 08-17-2021 (NCEI Accession 0247461) [Data set]. NOAA National Centers for Environmental Information. https://doi.org/10.25921/P8QE-ME08 https://doi.org/10.25921/p8qe-me08

Mignot, A., Ferrari, R., & Claustre, H. (2018). Floats with bio-optical sensors reveal what processes trigger the North Atlantic bloom. *Nature Communications*, *9*(1). https://doi.org/10.1038/s41467-017-02143-6

Millero, F. J., Lee, K., & Roche, M. (1998). Distribution of alkalinity in the surface waters of the major oceans. *Marine Chemistry*, *60*, 111–130.

Ocean Observatories Initiative Science Prospectus: Scientific Objectives and Network Design. (2007). https://io.ocean.washington.edu/files/science_prospectus_2007-10-10_lowres_0.pdf.

OOI Data Product Specification for Water Temperature. (2013). https://oceanobservatories.org/wp-content/uploads/2023/09/1341-00130_Data_Product_Spec_TEMPSFL_OOI-2.pdf

OOI Data Product Specification for Salinity. (2013). https://oceanobservatories.org/wp-content/uploads/2015/10/1341-00040_Data_Product_SPEC_PRACSAL_OOI.pdf

Olsen, A., Key, R. M., Van Heuven, S., Lauvset, S. K., Velo, A., Lin, X., Schirnick, C., Kozyr, A., Tanhua, T., Hoppema, M., Jutterström, S., Steinfeldt, R., Jeansson, E., Ishii, M., Pérez, F. F., & Suzuki, T. (2016). The global ocean data analysis project version 2 (GLODAPv2) - An

953 internally consistent data product for the world ocean. *Earth System Science Data*, *8*(2), 297–
954 323. https://doi.org/10.5194/essd-8-297-2016
955 Orr, J. C., Epitalon, J. M., Dickson, A. G., & Gattuso, J. P. (2018). Routine uncertainty
956 propagation for the marine carbon dioxide system. *Marine Chemistry*, *207*(October), 84–107.
957 https://doi.org/10.1016/j.marchem.2018.10.006
958 Painter, S. C., Henson, S. A., Forryan, A., Steigenberger, S., Klar, J., Stinchcombe, M. C.,
959 Rogan, N., Baker, A. R., Achterberg, E. P., & Moore, C. M. (2014). An assessment of the
960 vertical diffusive flux of iron and other nutrients to the surface waters of the subpolar North
961 Atlantic Ocean. *Biogeosciences*, *11*(8), 2113–2130. https://doi.org/10.5194/bg-11-2113-2014
962 Palevsky, H. I., Clayton, S., Atamanchuk, D., Battisti, R., Batryn, J., Bourbonnais, A., Briggs, E.
963 M., Carvalho, F., Chase, A. P., Eveleth, R., Fatland, R., Fogaren, K. E., Fram, J. P., Hartman,
964 S. E., Le Bras, I., Manning, C. C. M., Needoba, J. A., Neely, M. B., Oliver, H., … Wingard,
965 C. (2023). OOI Biogeochemical Sensor Data: Best Practices & User Guide. *The Global*
966 *Ocean Observing System*, *1.1.1*, 1–135. https://doi.org/10.25607/OBP-1865.2
967 Palevsky, H. I., & Doney, S. C. (2018). How Choice of Depth Horizon Influences the Estimated
968 Spatial Patterns and Global Magnitude of Ocean Carbon Export Flux. *Geophysical Research*
969 *Letters*, *45*(9), 4171–4179. https://doi.org/10.1029/2017GL076498
970 Palevsky, H. I., & Nicholson, D. P. (2018). The North Atlantic Biological Pump: Insights from
971 the Ocean Observatories Initiative Irminger Sea Array. *Oceanography*, *31*(1), 42–49.
972 https://doi.org/10.5670/oceanog.2018.108
973 Palevsky, H. I., & Quay, P. D. (2017). Influence of biological carbon export on ocean carbon
974 uptake over the annual cycle across the North Pacific Ocean. *Global Biogeochemical Cycles*,
975 *31*(1), 81–95. https://doi.org/10.1002/2016GB005527
976 Palevsky, H. I., Fogaren, K. E., Nicholson, D. P., Yoder, M. (2023b) Supplementary discrete
977 sample measurements of dissolved oxygen, dissolved inorganic carbon, and total alkalinity
978 from Ocean Observatories Initiative (OOI) cruises to the Irminger Sea Array 2018-2019.
979 Biological and Chemical Oceanography Data Management Office (BCO-DMO). (Version 1)
980 Version Date 2023-07-19. doi:10.26008/1912/bco-dmo.904722.1
981 Quay, P., Emerson, S., & Palevsky, H. (2020). Regional Pattern of the Ocean's Biological Pump
982 Based on Geochemical Observations. *Geophysical Research Letters*, *47*(14), 1–10.
983 https://doi.org/10.1029/2020GL088098
984 Quay, P., Stutsman, J., & Steinhoff, T. (2012). Primary production and carbon export rates
985 across the subpolar N. Atlantic Ocean basin based on triple oxygen isotope and dissolved O 2
986 and Ar gas measurements. *Global Biogeochemical Cycles*, *26*(2), 1–13.
987 https://doi.org/10.1029/2010GB004003
988 Racapé, V., Pierre, C., Metzl, N., Lo Monaco, C., Reverdin, G., Olsen, A., Morin, P., Vázquez-
989 Rodríguez, M., Ríos, A. F., & Pérez, F. F. (2013). Anthropogenic carbon changes in the
990 Irminger Basin (1981-2006): Coupling δ13C DIC and DIC observations. *Journal of Marine*
991 *Systems*, *126*, 24–32. https://doi.org/10.1016/j.jmarsys.2012.12.005
992 Sanders, R., Henson, S. A., Koski, M., De La Rocha, C. L., Painter, S. C., Poulton, A. J., Riley,
993 J., Salihoglu, B., Visser, A., Yool, A., Bellerby, R., & Martin, A. P. (2014). The Biological
994 Carbon Pump in the North Atlantic. *Progress in Oceanography*, *129*(PB), 200–218.
995 https://doi.org/10.1016/j.pocean.2014.05.005
996 Sathyendranath, S., Stuart, V., Nair, A., Oka, K., Nakane, T., Bouman, H., Forget, M. H., Maass,
997 H., & Platt, T. (2009). Carbon-to-chlorophyll ratio and growth rate of phytoplankton in the
998 sea. *Marine Ecology Progress Series*, *383*, 73–84. https://doi.org/10.3354/meps07998

Sauvé, J., Gray, A. R., Prend, C. J., Bushinsky, S. M., & Riser, S. C. (2023). Carbon Outgassing in the Antarctic Circumpolar Current Is Supported by Ekman Transport From the Sea Ice Zone in an Observation-Based Seasonal Mixed-Layer Budget. Journal of Geophysical Research: Oceans, 128(11). https://doi.org/10.1029/2023JC019815

Siegel, D. A., DeVries, T., Cetinić, I., & Bisson, K. M. (2023). Quantifying the Ocean's Biological Pump and Its Carbon Cycle Impacts on Global Scales. *Annual Review of Marine Science*, *15*, 329–356. https://doi.org/10.1146/annurev-marine-040722

Smith, L. M., Barth, J. A., Kelley, D. S., Plueddemann, A., Rodero, I., Ulses, G. A., Vardaro, M. F., & Weller, R. (2018). The Ocean Observatories Initiative. *Oceanography*, *31*(1), 16–35. https://doi.org/10.5670/oceanog.2018.105

Stemmann, L., & Boss, E. (2012). Plankton and Particle size and Packaging: From Determining Optical Properties to Driving the Biological Pump. *Annual Review of Marine Science*, *4*, 263–290. https://doi.org/10.1146/annurev-marine-120710-100853

Sterl, M. F., & de Jong, M. F. (2022). Restratification Structure and Processes in the Irminger Sea. *Journal of Geophysical Research: Oceans*, 127(12). https://doi.org/10.1029/2022JC019126

Sverdrup, H. U. (1953). On conditions for the vernal blooming of phytoplankton. *J. Cons. Int. Explor. Mer*, 18(3), 287-295.

Takahashi, T., Sutherland, S. C., Sweeney, C., Poisson, A., Metzl, N., Tilbrook, B., Bates, N., Wanninkhof, R., Feely, R. A., Sabine, C., Olafsson, J., & Nojiri, Y. (2002). Global sea–air CO_2 flux based on climatological surface ocean pCO_2, and seasonal biological and temperature effects. *Deep Sea Research Part II: Topical Studies in Oceanography*, *49*, 1601–1622.

Uppström, L. R. (1974). The boron/chlorinity ratio of deep-sea water from the Pacific Ocean. *Deep-Sea Research*, *21*, 161–162. https://archive.org/details/sim_deep-sea-research_1974_21

U.S. Integrated Ocean Observing System, 2020. QARTOD - Prospects for Real-Time Quality Control Manuals, How to Create Them, and a Vision for Advanced Implementation. 22 pp. DOI: 10.25923/ysj8-5n28

Våge, K., Pickart, R. S., Moore, G. W. K., & Ribergaard, M. H. (2008). Winter mixed layer development in the central Irminger Sea: The effect of strong, intermittent wind events. *Journal of Physical Oceanography*, *38*(3), 541–565. https://doi.org/10.1175/2007JPO3678.1

Van Heuven, S., Pierrot, D., Rae, J. W. B., Lewis, E., & Wallace, D. W. R. (2011). MATLAB Program Developed for CO_2 System Calculations. ORNL/CDIAC-105b. [Software]. Carbon Dioxide Information Analysis Center (CDIAC). https://doi.org/10.3334/CDIAC/OTG.CO2SYS_MATLAB_V1.1

Volk, T., & Hoffert, M. I. (1985). Ocean Carbon Pumps: Analysis of Relative Strength and Efficiencies in Ocean-Driven Atmospheric CO_2 Changes. *The Carbon Cycle and Atmospheric CO_2: Natural Variations Archean to Present*.

Wanninkhof, R. (1992). Relationship between wind speed and gas exchange over the ocean. *Journal of Geophysical Research*, *97*(C5), 7373–7382. https://doi.org/10.1029/92JC00188

Wanninkhof, R. (2014). Relationship between wind speed and gas exchange over the ocean revisited. *Limnology and Oceanography: Methods*, *12*(JUN), 351–362. https://doi.org/10.4319/lom.2014.12.351

Weiss, R. F. (1974). Carbon Dioxide in water and seawater: The solubility of a non-ideal gas. *Marine Chemistry*, *2*, 203–215. https://doi.org/10.5194/bg-13-841-2016

Yang, B., Shadwick, E. H., Schultz, C., & Doney, S. C. (2021). Annual Mixed Layer Carbon Budget for the West Antarctic Peninsula Continental Shelf: Insights From Year-Round Mooring Measurements. *Journal of Geophysical Research: Oceans*, *126*(4), 1–15. https://doi.org/10.1029/2020JC016920